INORGANIC CHEMISTRY FRONTIERS

RESEARCH ARTICLE

View Article Online
View Journal | View Issue

Check for updates

Cite this: *Inorg. Chem. Front.*, 2024, **11**, 1186

A novel multi-carboxyl functionalized MOF platform for effective photodynamic therapy with hypoxia modulation based on prominent self-oxygen generation†

Guorui Gao,‡[a] Yifan Wang,‡[a] Yu Jiang,[a] Shiping Luo,[a] Mengnan Li,[a] Yanyu Cao,[a] Yu Ma*[a] and Bo Tang *[a,b]

Received 22nd November 2023,
Accepted 2nd January 2024

DOI: 10.1039/d3qi02416d

rsc.li/frontiers-inorganic

Photodynamic therapy (PDT) has emerged as an important minimally invasive tumor treatment technology. The use of metal–organic frameworks (MOFs) that integrate porphyrin photosensitizers into the ordered porous structure has opened up an attractive way to inhibit the photoinduced quenching of the photosensitizer and effectively enhance PDT. However, as a reactive oxygen species (ROS)-based therapy, the efficacy of PDT is still inhibited by the hypoxic tumor microenvironment. Here, we propose that the fabrication of a novel multifunctional MOF platform with both clinically available iron catalase-like active centers and near-infrared photosensitive molecules with a higher excitation wavelength can effectively improve the photodynamic performance of this type of photosensitive platform. To overcome the challenge of lack of water-stable iron-based MOFs simultaneously containing large open channels and high density redox metal centers, we for the first time, using a multicarboxyl modification strategy, integrated high density Fe-based catalytic centers and the clinically available ICG molecule into the same MOF and obtained a novel self-oxygen generation enhanced photodynamic platform ICG ⊂ UMOF@FeOOH (IMF). The effectively enhanced PDT performance of this novel platform based on a multifunctional MOF under hypoxia conditions was successfully verified using HeLa cells and *in vivo* anti-tumor experiments.

Published on 03 oajagemánnu 2024. Downloaded on 2026-02-01 22:11:29.

Introduction

Photodynamic therapy (PDT), as a non-invasive but effective cancer treatment method, has attracted extensive attention.[1] It fights solid tumors by transferring energy from the excited photosensitizer (PS) upon irradiation to the tissue oxygen (O_2) to change the level of reactive oxygen species (ROS).[2] At present, PDT based on limited varieties of PSs has been clinically approved for different types of tumor treatment.[3] However, owing to the high oxygen consumption induced by the rapid proliferation of tumor cells and hypoxia supply caused by tumor vascular system malformation, the hypoxic microenvironment has become one of the typical features of solid tumors.[4] During PDT treatment, oxygen consumption will further aggravate hypoxia, thereby limiting the PDT efficiency.[5] To solve this problem, more and more oxygen carrying[6,7] or oxygen generating[8–11] materials have been developed to improve tumor hypoxia. In particular, catalase catalysts can effectively decompose the highly expressed H_2O_2 into O_2 in the endogenous tumor microenvironment, and further enhance the PDT efficiency. However, the instability of catalase has prompted people to constantly strive to develop more outstanding enzyme-like systems.[12–14]

As an emerging porous material formed by the self-assembly of metal ions or clusters with organic bridging ligands, metal–organic frameworks (MOFs) have attracted extensive attention.[15] Based on their unique advantages such as adjustable composition, designable structure, high porosity, easy functionalization and good biocompatibility, these kinds of porous materials have presented attractive research prospects in separation,[16–18] sensing,[19,20] drug loading[21] and enzyme-like catalysis.[22–26] Among them, MOFs based on metalloporphyrin linkers have been used as excellent catalase-like enzymes, such as in a series of oxidation reactions, or biomimetic catalysts.[27–30] Meanwhile, MOFs as porous carriers,

[a]College of Chemistry, Chemical Engineering and Materials Science, Collaborative Innovation Center of Functionalized Probes for Chemical Imaging in Universities of Shandong, Key Laboratory of Molecular and Nano Probes, Ministry of Education, Institute of Molecular and Nano Science, Shandong Normal University, Jinan 250014, P. R. China. E-mail: may@sdnu.edu.cn, tangb@sdnu.edu.cn
[b]Laoshan Laboratory, Qingdao, 266200, P. R. China

† Electronic supplementary information (ESI) available: Materials and methods, SEM and TEM images, DLS data, SEM-mapping images, PXRD patterns, UV-vis absorption spectra, and zeta potential diagram. See DOI: https://doi.org/10.1039/d3qi02416d

‡ These authors contributed equally to this work.

This journal is © the Partner Organisations 2024

Published on 03 oajagemánnu 2024. Downloaded on 2026-02-01 22:11:29.

especially as effective porphyrin photosensitizer carriers, have achieved great progress in PDT.[31] Our group has also constructed an extremely effective delivery platform with the maximum loading capability of porphyrin PSs at that time as the first signal molecule H_2S activable MOF PS for PDT against cancer.[32] However, although porphyrin PSs have been used in the clinic, the tissue penetration depth of exciting light is limited, and continuous oxygen consumption further limits their PDT efficiency. Considering the fact that coordinated iron ions show artificial enzyme activity[27] and iron-based materials have shown unique biological safety,[33] such as Fe_3O_4 as a clinical MRI contrast agent for many years,[34,35] the development of MOFs that contain both effective iron catalytic centers and efficient loading performance for other biocompatible near-infrared photosensitive molecules with a higher excitation wavelength becomes of great significance for further self-oxygen generation enhanced PDT efficiency. However, the fabrication of multifunctional iron-based MOFs with good water stability even under low pH conditions, a suitable nanometer size and high efficiency for large size guest molecular loading performance is still a challenge.

Zirconium-based MOFs have been regarded as a type of representative example showing extraordinary stability, owing to the strong interaction between Zr(IV) and carboxylate.[36] With high porosity and a suitable nanometer size, nanoscale UiO-66 as a representative of zirconium-based MOFs has been employed to load with customized components inside their pores and can even incorporate active sites within their framework by functionalization of ligands.[37–40] Herein, we projected that introducing iron ions into the rich uncoordinated carboxyl functionalized metal–organic framework UiO-66-$(COOH)_2$ (UMOF) could enable this stable platform to be suitable for effective self-oxygen generation enhanced PDT, due to its excellent stability, conveniently and highly loaded catalytic active centers and pore confined biocompatible photosensitive molecule with a higher excitation wavelength.

Specifically, the uncoordinated multi-carboxyl functionalized UMOF, which maintained a 3D porous framework as exceptionally stable UiO-66 including Zr_6 clusters $Zr_6O_4(OH)_4(CO_2)_{12}$,[41] was first synthesized based on the polycarboxyl ligand 1,2,4,5-benzenetetracarboxylic acid. Then, with this UMOF as a functional regulation unit and carrier, the biocompatible iron catalytic center and the clinically available indocyanine green (ICG)[42] as a photosensitive molecule with a higher excitation wavelength were combined to obtain a novel self-oxygen generation enhanced photodynamic nanoplatform ICG ⊂ UMOF@FeOOH (IMF). Among them, while the carboxyl groups of the UMOF coordinated with iron ions in the solution, the nucleation of biocompatible iron oxide FeOOH on the UMOF was inevitably promoted simultaneously. The coordinated Fe^{3+} formed by the polycarboxyl groups acted as high density active catalase-like sites to enhance the oxygen generation capability of IMF. After uptake by cancer cells, the Fe^{3+} in IMF could effectively decompose H_2O_2 to generate O_2, which could be further converted into cytotoxic $^1O_2$ by ICG, and finally the self-oxygen generation enhanced photodynamic performance was successfully realized. The details of this strategy are illustrated in Fig. 1.

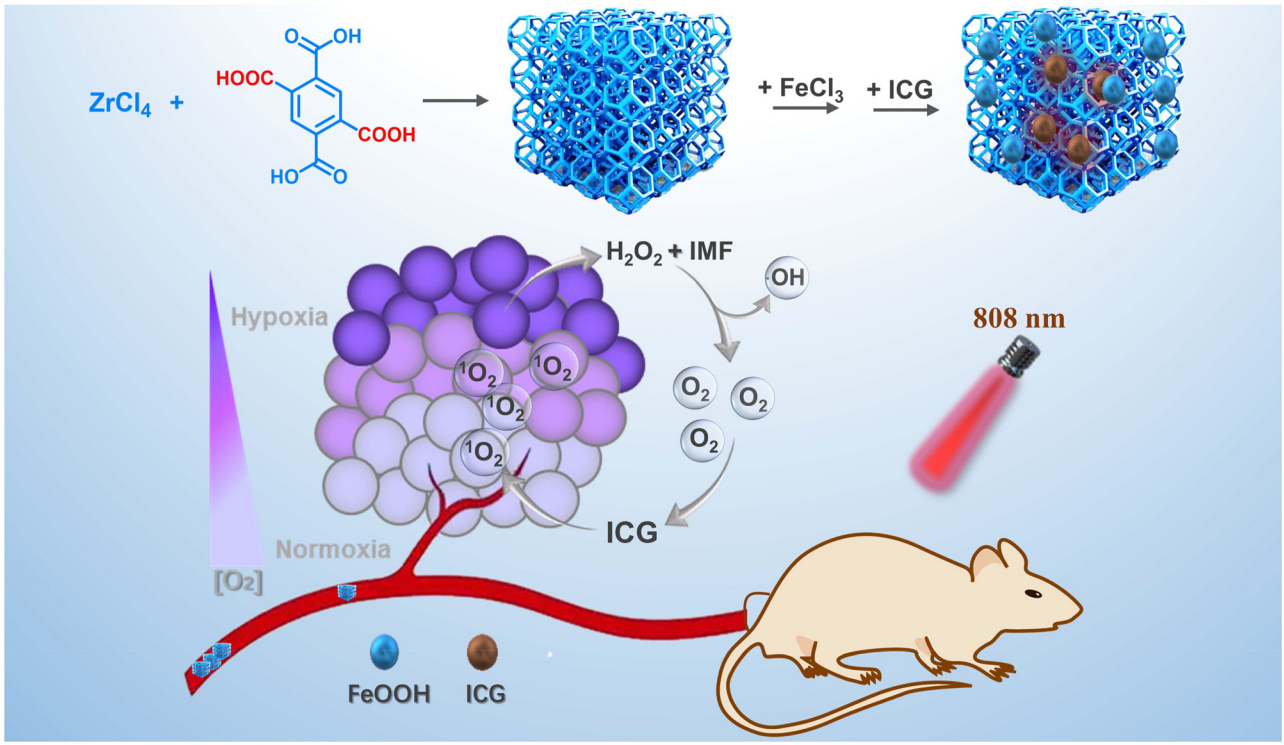

Fig. 1 An illustration of the design and construction strategy for IMF.

Published on 03 oajagemánnu 2024. Downloaded on 2026-02-01 22:11:29.

Experimental section

Synthesis of UMOF

Carboxyl functionalized UMOF was synthesized by mixing the multi-carboxyl ligand 1,2,4,5-benzenetetracarboxylic acid (2.15 g, 8.46 mmol) and $ZrCl_4$ (1.15 mg, 4.93 mmol) in 25 mL of boiling water for 24 h.[43] After collection and washing with hot water, the crude products in hot water were further heated at 100 °C for another 16 h. Finally, the nanoscale crystals were collected and washed with acetone several times and then dried in a vacuum for 24 h.

Synthesis of MF

The UMOF was dispersed in 5 mL of water and then 25.92 mg of $FeCl_3{\cdot}6H_2O$ was added. The mixture was then stirred for 12 h at 60 °C. After cooling to room temperature, the product MF was collected by centrifugal separation and washed with water three times.

Synthesis of IMF

5 mg of MF was added to a solution of ICG (5 mL, 0.4 mg mL^{-1}) and stirred for 12 h at room temperature. Then, the final product IMF was collected by centrifugal separation and washed with water several times.

Synthesis of FeOOH

3.243 g of $FeCl_3{\cdot}6H_2O$ was dispersed in 60 mL of water and then stirred for 5 h at 70 °C. After cooling to room temperature, the product FeOOH was collected by centrifugal separation and washed with water three times.

Methylene blue degradation assay

600 μg of IMF was uniformly dispersed in acetic acid/sodium acetate buffer solution (pH = 5.0), and then 100 μL of 0.1 mg mL^{-1} methylene blue solution and 10 μL of H_2O_2 (200 μM) were added sequentially. After incubation at 37 °C under dark conditions, the absorption spectra of methylene blue were recorded using a UV-vis spectrophotometer.

Catalase-like activity of IMF

500 μg of IMF was first dispersed uniformly in acetic acid/sodium acetate buffer solution (pH 5.0). After 1.67 mM H_2O_2 was added, the solution was incubated at 37 °C under dark conditions. Then, the supernatant obtained by centrifugation was mixed with $Ti(SO_4)_2$ solution and its UV-vis absorbance at 405 nm was measured. The control groups without IMF were also performed based on the above methods.

Oxygen generation

500 μg of IMF was first dispersed uniformly in acetic acid/sodium acetate buffer solution (pH = 5.0). After 16.7 mM H_2O_2 was added, the mixture was heated at 50 °C for 20 min and the formation of oxygen bubbles could be clearly observed.

The ability of O_2 generation was further monitored using 1,3-diphenylisobenzofuran (DPBF). 400 μg of IMF, 1 mM RDPP probe and 200 μM H_2O_2 were mixed in acetic acid/sodium acetate buffer solution (pH = 5.0), and the fluorescence spectra of RDPP were simultaneously recorded.

$^1O_2$ generation

The ability of $^1O_2$ generation of IMF was monitored using 1,3-diphenylisobenzofuran (DPBF). 400 μg of IMF was first incubated with 1.67 mM H_2O_2 in acetic acid/sodium acetate buffer solution (pH = 5.0). After DPBF (120 μM) was added, the above solution was irradiated with 808 nm laser light (1.5 W cm^{-2}). The UV-vis spectra were simultaneously recorded. In addition, the control experiment was carried out under similar conditions as mentioned earlier, except for the absence of H_2O_2.

Cell culture

HeLa cells were maintained following the protocols provided by the American Type Tissue Culture Collection. HeLa cells were seeded in a confocal dish and incubated in high-glucose Dulbecco's modified Eagle's medium (DMEM) containing 10% fetal bovine serum and 1% antibiotics (penicillin/streptomycin). Then, the cells were cultured at 37 °C in a humidified incubator containing 21% O_2 and 5% CO_2. To mimic the hypoxic environment, the cells were also cultured with 2% O_2 and 5% CO_2 at 37 °C.

MTT assay

The cytotoxicity of IMF was evaluated by employing HeLa cells. HeLa cells were seeded in 96-well plates (200 μL per well). After incubation for 24 h, these HeLa cells were cocultured respectively with IMF or IMF + H_2O_2 for another 6 h under normoxia (21% O_2) or hypoxia (2% O_2) conditions. Next, the cells of the corresponding groups were irradiated with 808 nm laser light (1.5 W cm^{-2}, 5 min). Then, the medium was removed and the MTT solution was delivered into all wells. After 4 h, the MTT solution was removed and 200 μL of DMSO was added to dissolve the formazan crystals. The absorbance was monitored at 490 nm using a microplate reader.

Western blot assay

After culturing for the first 24 h, anaerobic incubation (2% O_2) of HeLa cells was performed for another 4 h. Then, IMF + H_2O_2 was delivered into the hypoxia cells in DMEM containing 10% FBS for another 4 h. Subsequently, the cells were collected and lysed in radioimmunoprecipitation assay buffer with phenylmethanesulfonyl fluoride. Then, the protein analysis was performed using the BCA protein quantification kit. After quantification and electrophoresis separation, the protein was transferred to a poly(vinylidene difluoride) membrane and the membrane was then incubated with the rabbit HIF-1α monoclonal antibody at 4 °C overnight. Next, the poly(vinylidene difluoride) membrane was further placed in the horseradish peroxidase-conjugated affinipure goat anti-rabbit IgG(H + L) antibody for 1 h. Finally, a gel imaging system (Bio-Rad ChemiDoc™ XRS+) was employed to observe the results.

 This journal is © the Partner Organisations 2024

Published on 03 oajagemánnu 2024. Downloaded on 2026-02-01 22:11:29.

Confocal imaging

Intracellular oxygen generation. Three groups of HeLa cells were seeded in confocal dishes for 24 h. After 4 hours of anaerobic incubation, H_2O_2 or IMF + H_2O_2 was delivered into the cells in DMEM containing 10% FBS at 37 °C under hypoxia conditions (2% O_2) for another 4 h. Next, the different groups of cells were all incubated with the RDPP probe under hypoxia (2% O_2) conditions for 35 minutes in the dark. After washing with PBS, the fluorescence images of the cells were immediately recorded using a confocal laser scanning microscope (CLSM). The excitation wavelength was 488 nm, and the emission was collected between 500 and 800 nm.

Intracellular ROS generation. Eight groups of HeLa cells were seeded in confocal dishes for 24 h. Then, IMF or IMF + H_2O_2 was delivered into the cells in DMEM containing 10% FBS at 37 °C under normoxia (21% O_2) (groups 1–4) or hypoxia (2% O_2) (groups 5–8) conditions for another 6 h. Next, the eight groups of cells were all incubated with the DCFH-DA probe under the corresponding normoxia (21% O_2) or hypoxia (2% O_2) conditions for 30 minutes. While groups 1, 2, 5 and 6 were cultured in the dark, irradiation treatment was further performed on groups 3, 4, 7 and 8 with an 808 nm laser (1.5 W cm^{-2}) for 5 min. After washing with PBS, the fluorescence images of the cells were immediately recorded using a confocal laser scanning microscope (CLSM). The excitation wavelength was 488 nm and the emission was collected between 500 and 600 nm. The corresponding fluorescence intensity was the average fluorescence intensity of the cell area from the confocal fluorescence images, which was quantified using LAS X software.

Photodynamic performance. Sixteen groups of HeLa cells were seeded and cultured in confocal dishes for 24 h at 37 °C. Then, IMF or IMF + H_2O_2 was delivered into the cells in DMEM containing 10% FBS at 37 °C under normoxia (21% O_2) (groups 1–8) or hypoxia (2% O_2) (groups 9–16) conditions for another 6 h. While groups 1, 2, 5 and 6 were cultured under normoxia conditions and groups 9, 10, 13 and 14 were cultured under hypoxia conditions in the dark, irradiation treatment was further performed on groups 3, 4, 7 and 8 under normoxia conditions and groups 11, 12, 15 and 16 with an 808 nm laser (1.5 W cm^{-2}) for 10 min. Subsequently, the sixteen groups of cells were all stained with the mixture of calcein-AM and PI at 37 °C for 30 min. After washing with PBS three times, the fluorescence images of the cells were immediately recorded using a confocal laser scanning microscope (CLSM). The excitation wavelengths for calcein-AM and PI were 488 nm and 561 nm, and the corresponding emission was collected between 500–560 nm and 580–650 nm, respectively.

Flow cytometry

HeLa cells were seeded and cultured in 6-well plates for 24 h at 37 °C. Then, IMF or IMF + H_2O_2 was delivered into the cells under hypoxia (2% O_2) conditions for another 6 h. The cells of the corresponding groups were irradiated with an 808 nm laser (1.5 W cm^{-2}) for 5 min, while the other groups were incubated in the dark. Subsequently, after the cells were all stained with annexin V-FITC and PI, flow cytometric analysis was performed.

Animal tumor xenograft models

All animal experiments were carried out according to the Principles of Laboratory Animal Care (People's Republic of China) and the Guidelines of the Animal Investigation Committee, Biology Institute of Shandong Academy of Science, China. Female nude mice (4–6 weeks old, ~16 g) were purchased from Changzhou Cavens Experimental Animal Co., Ltd and housed under normal conditions with free access to food and water *ad libitum*. A HeLa tumor model was established by subcutaneous injection of HeLa cells (8×10^6 cells per mouse, 50 μL PBS) into the right flank of nude mice. When the tumor volume (V) reached about 75–100 mm^3, intratumoral administration was performed. In addition, the tumor volume (V) was determined by measuring the length (L) and width (W), and is calculated as $V = (W^2 \times L)/2$. The relative tumor volumes were calculated for each mouse as V/V_0 (V_0 was the tumor volume when the treatment was initiated).

Animal tumor xenograft models

In vivo antitumor efficacy assay was performed on HeLa tumor-bearing nude mice. The mice with a tumor volume of 75–100 mm^3 were randomly divided into three different treatments (mice in each group $n \geq 3$): group 1, intratumor injection of PBS (50 μL) only; group 2, injection of IM in PBS (50 μL, C_{ICG} = 0.5 mg kg^{-1}) combined with light irradiation; and group 3, injection of IMF in PBS (50 μL, C_{ICG} = 0.5 mg kg^{-1}) combined with light irradiation. PDT treatment was performed on group 3 by irradiating the tumor region with near infrared laser irradiation (808 nm, 1.5 W cm^{-2}) for 5 min. The tumor volume and the body weights of the mice were monitored once every two days for 10 days (day 0, 2, 4, 6, 8 and 10).

Results and discussion

Synthesis and characterization of IMF

In the construction of the IMF, UMOF was first synthesized by the reaction of 1,2,4,5-benzenetetracarboxylic acid and $ZrCl_4$ in boiling water. Then, $FeCl_3 \cdot 6H_2O$ as an iron source was selected to obtain catalytically active sites. While the carboxyl groups of the UMOF coordinated with iron ions in the solution, the nucleation of FeOOH on the UMOF was inevitably promoted simultaneously and thereby MF with FeOOH loading formed. After the photosensitive molecule ICG was included in MF at room temperature, the target product IMF was obtained. The framework structure of UMOF before and after loading FeOOH and ICG were first checked by powder X-ray diffraction (PXRD) characterization. As shown in Fig. 2A, the diffraction peaks of UMOF fitted well with that simulated by UiO-66, which proved that these two MOFs possess the same framework structure. The Fourier transform infrared (FT-IR) spectra of IMF displayed the characteristic bands of the carboxylate groups. The

Published on 03 oajagemánnu 2024. Downloaded on 2026-02-01 22:11:29.

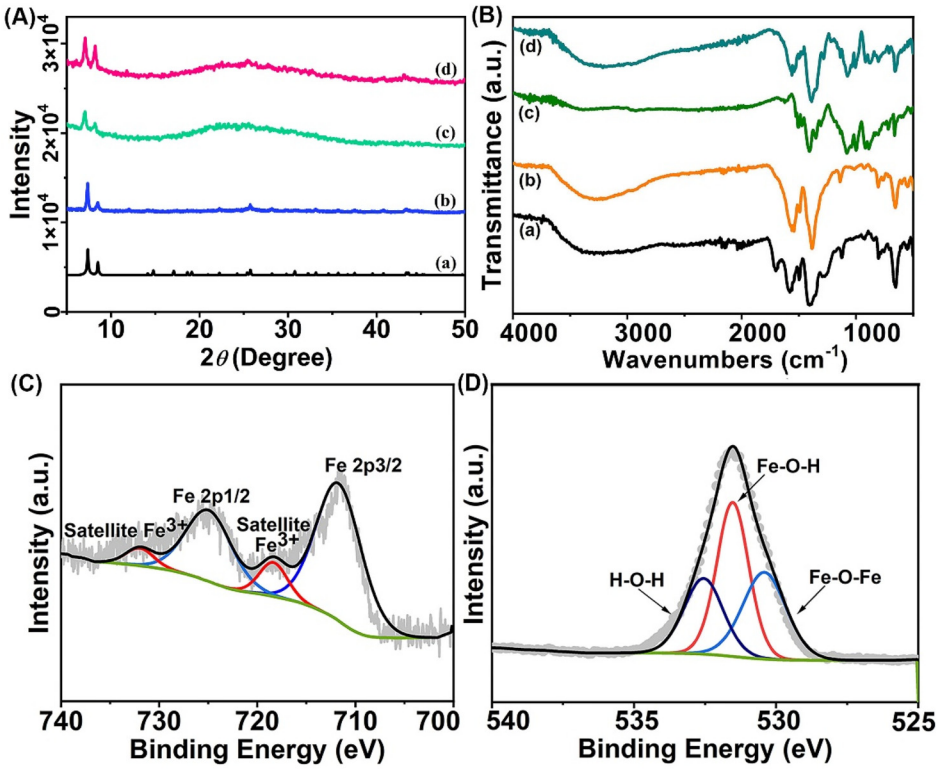

Fig. 2 (A) PXRD patterns of (a) UiO-66, (b) UMOF, (c) MF, and (d) IMF; (B) FT-IR spectra of (a) UMOF, (b) MF, (c) ICG, and (d) IMF; (C) Fe 2p XPS spectra of IMF (the grey spiked curve was the initial curve of XPS and the other solid lines were the corresponding fitting curves); and (D) O 1s XPS spectra of IMF (the grey dotted curve was the initial curve of XPS and the other solid lines were the corresponding fitting curves).

strong bands at about 1700 cm^{-1} were attributable to the uncoordinated carboxyl groups (Fig. 2B). Additionally, the PXRD patterns of MF (UMOF@FeOOH) and IMF also matched well with that of UMOF, which demonstrated that the structure of UMOF remains unchanged before and after loading FeOOH and ICG (Fig. 2A). However, no obvious diffraction peaks of crystalline FeOOH were observed from the PXRD diagram of IMF. Next, to confirm that the amorphous FeOOH had been successfully incorporated into the UMOF, X-ray photoelectron spectroscopy (XPS) spectra of Fe 2p and O 1s for IMF were collected.[44] As depicted in Fig. 2C, two obvious characteristic peaks at 711.6 eV (Fe 2p3/2) and 725.0 eV (Fe 2p1/2) corresponding to 2p3/2 and 2p1/2 of Fe^{3+} with two shake-up satellites at 719.5 eV and 732.9 eV were observed, which was consistent with that of FeOOH.[45] In the XPS spectra of O 1s (Fig. 2D), the peaks at 531.5 eV for the Fe–O–H bond and 530.4 eV for the Fe–O–Fe bond could further demonstrate the presence of FeOOH.[45]

To verify the successful loading of ICG, UV-vis absorption, fluorescence and FT-IR spectra of IMF were obtained. As shown in Fig. S1,† compared with the UV-vis absorption spectra of UMOF and FeOOH, the new absorption peak of IMF at 880 nm should be attributed to the loaded ICG, which presented a red shift compared with that of free ICG. And the amount of ICG incorporated into the framework was calculated to be about 6.25 wt% (Fig. S2†). Similarly, the fluorescence peak of ICG could also be observed from the fluorescence spectrum of IMF (Fig. S3†). To further certificate the successful loading of ICG, FT-IR spectrum of IMF was recorded. As shown in Fig. 2B, compared with the FT-IR spectra of UMOF and MF, the new absorption band appearing at about 1000 cm^{-1} in line d proved the successful loading of ICG. Additionally, the characteristic peak of the uncoordinated COOH group at 1700 cm^{-1} disappeared in line b and d for MF and IMF, which indicated that FeOOH integrated with UMOF by coordination interactions between the Fe^{3+} and carboxyl groups.

Next, transmission electron microscopy (TEM) and scanning electron microscopy (SEM) were employed to characterize the morphology of the materials (Fig. S4 and S5†). As shown in Fig. S4,† IMF displayed a uniform morphology similar to that of UMOF and presented good dispersibility. The dynamic light scattering data showed that the hydrated particle size of these materials increased slightly after loading FeOOH and ICG in turn, and the average hydration particle size of the final synthesized IMF is about 243.18 nm (Fig. S6†). Additionally, in Fig. S7,† the corresponding elemental mappings obtained from energy-dispersive spectroscopy of IMF also proved the successful loading of ICG and FeOOH. Despite the fact that both XPS and EDS mapping characterization affirming the

 This journal is © the Partner Organisations 2024

Published on 03 oajagemánnu 2024. Downloaded on 2026-02-01 22:11:29.

existence of FeOOH and that the molar ratio of iron to oxygen is 1 : 3, the morphology of FeOOH has not been clearly observed from the electron microscopy images. To intuitively reveal the morphology of FeOOH, larger-sized UiO-66-$(COOH)_2$ with more regular shape (UMOF-c) loaded with FeOOH (MF-c) were synthesized. The framework structures of UMOF-c and MF-c were first checked by PXRD characterization, which proved that these MOFs with different sizes possess the same framework structure (Fig. S8† and Fig. 2A). From the TEM images in Fig. S9 and S10,† we could clearly see the formation of spindle FeOOH, which is consistent with the morphology of separately synthesized ferric hydroxide according to the literature (Fig. S11†).[45] To further prove that MF-c and MF have similar composition, the UV-vis absorption spectra of MF and MF-c were collected. The characteristic absorption peak of FeOOH at 366 nm can be observed in the UV-vis absorption spectrum of MF and MF-c, though the intensity for MF is weaker than that of MF-c with an obviously more FeOOH loading (Fig. S12 and S13†). Zeta potential diagrams for UMOF, MF and IMF were also obtained. As shown in Fig. S14,† the zeta potential of the material also changed after FeOOH and ICG were loaded. All the above results further demonstrated that we have successfully synthesized IMF with simultaneously loading FeOOH and ICG. Then, the stability of IMF was evaluated. As shown in Fig. 2A and Fig. S15,† after immersion in PBS buffer and the acetic acid/sodium acetate buffer aqueous solution for 24 hours, the PXRD patterns were still in good agreement with that of UiO-66, proving that IMF has sufficient stability under Fenton reaction and physiological conditions.

Catalase-like activity of IMF

To evaluate the catalase-like activity of IMF, the titanium sulfate colorimetric method was selected to detect the consumption of H_2O_2.[46] First, an optimum loading amount of FeOOH was optimized according to the catalytic performance (Fig. S16†), and the IMF synthesized with 40 mg of UMOF displaying the highest degradation rate has been selected as the final material for the corresponding catalytic performance characterization. As displayed in Fig. 3A, compared with single FeOOH, the catalytic activity of IMF material was improved significantly. After adding KSCN to the supernatant of reaction solution obtained by centrifugation, there was no color change, indicating that Fe^{3+} in the solid IMF was the catalytic active center. We could also see that the H_2O_2 degradation rate of MF and IMF at 300 min was almost the same, which indicated that the ICG loading has no significant impact on the catalase-like activity of IMF. Simultaneously, we could find obvious bubbles generated in the H_2O_2 degradation experiment of IMF (Fig. 3A inset). $[Ru(dpp)_3]Cl_2$ (RDPP) probe was then selected to further verify that the gas generated is O_2.[47] With the generation of O_2, the fluorescence intensity of RDPP at 615 nm decreased continuously (Fig. 3B). Based on the above phenomenon, we inferred that high density active catalase-like sites were formed on the interface between FeOOH and UMOF, and functionalized polycarboxyl groups of UMOF

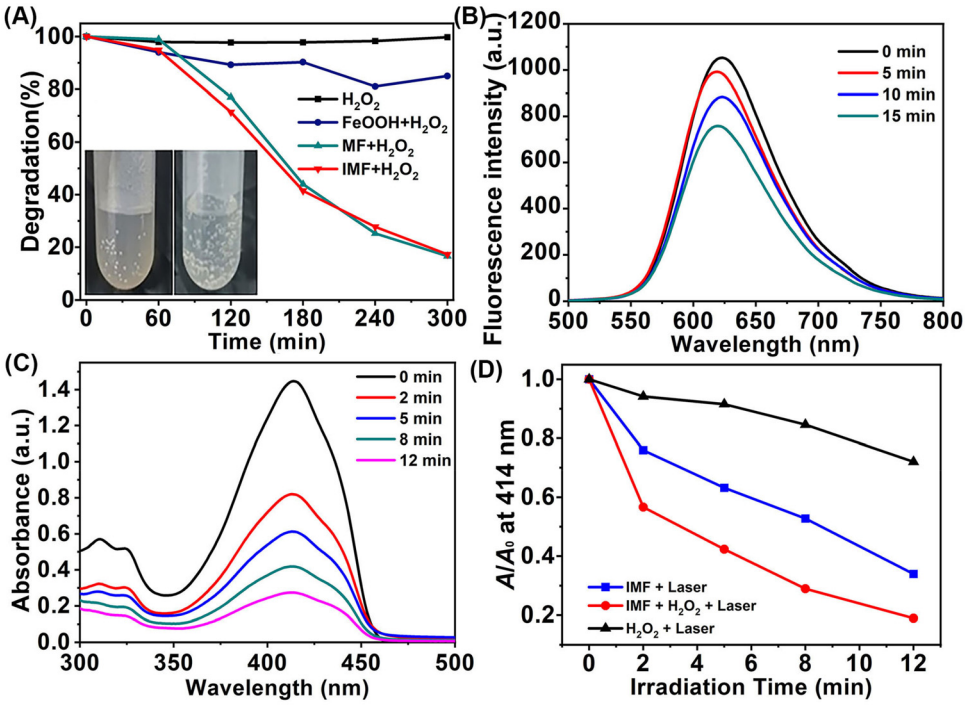

Fig. 3 (A) H_2O_2 degradation after treatment with FeOOH, MF and IMF; (B) fluorescence spectra of RDPP in IMF + H_2O_2 solution at different time points; (C) UV-vis absorption spectra of DPBF in IMF + H_2O_2 solution upon irradiation (808 nm, 1.5 W cm^{-2}); and (D) the relative absorbance of DPBF at 410 nm after irradiation for different times in H_2O_2, IMF and IMF + H_2O_2 solution. A_0 is the initial absorbance of the DPBF probe.

Published on 03 oajagemánnu 2024. Downloaded on 2026-02-01 22:11:29.

carrier fortunately increased the effective concentration of Fe^{3+} active site through the coordination effect to the enhanced oxygen generation capability of IMF.

Oxygen and singlet oxygen generation of IMF

To further demonstrate the effective self-oxygen generation enhanced photodynamic performance of IMF *in vitro*, 1,3-diphenylisobenzofuran (DPBF) as a $^1O_2$ probe[48] was first employed to verify the generation of ROS. As shown in Fig. 3C, with infrared light irradiation (808 nm, 1.5 W cm^{-2}), the absorption intensity of DPBF decreased more quickly within 2 min in the co-presence of IMF and H_2O_2. After extending the irradiation time, the $^1O_2$ production performance of the material will be further improved in cooperation with synergistic oxygen generation, and IMF can achieve more than 80% DPBF degradation within 12 min. As shown in Fig. 3D and Fig. S17,† the degradation efficiency of hydrogen peroxide is significantly higher than that of other control groups (IMF + laser and H_2O_2 + laser). The above results showed that the remarkable enhanced O_2 generation performance of FeOOH based on the UMOF can effectively and synergistically improve the ability of $^1O_2$ generation. Furthermore, to prove the ability of IMF in alleviating hypoxia on account of the self-oxygen generation performance of IMF in the living cells, western blot assay for the level analysis of hypoxia-inducible factor-1α (HIF-1α) and CLSM studies based on RDPP staining were performed. As we all know, HIF-1α was typically upregulated under hypoxic conditions and the supply of O_2 could induce HIF-1α degradation. As shown in Fig. S18,† compared with the control group, IMF could indeed obviously downregulate the level of HIF-1α. Meanwhile, the oxygen generation capacity of IMF in the living cells was also observed by CLSM studies. As can be seen from Fig. S19,† after the cells were incubated with 200 μg mL^{-1} IMF in the dark, the intensity of green fluorescence of RDPP (1 mM) decreased obviously in the presence of H_2O_2 under hypoxia conditions compared with the corresponding control groups, indicating the oxygen generation capacity of IMF in living cells.

Subsequently, the ROS generation capacity of IMF in the living cells was evaluated by a reactive oxygen species indicator 2′,7′-dichlorodihydrofluorescein diacetate (DCFH-DA).[49] Confocal fluorescence microscopy studies were performed on human cervical carcinoma (HeLa) cells. As shown in Fig. 4A–C, when the cells were incubated with 200 μg mL^{-1} IMF with near infrared light irradiation (808 nm, 1.5 W cm^{-2}), the intensity of green fluorescence increased most significantly in the pres-

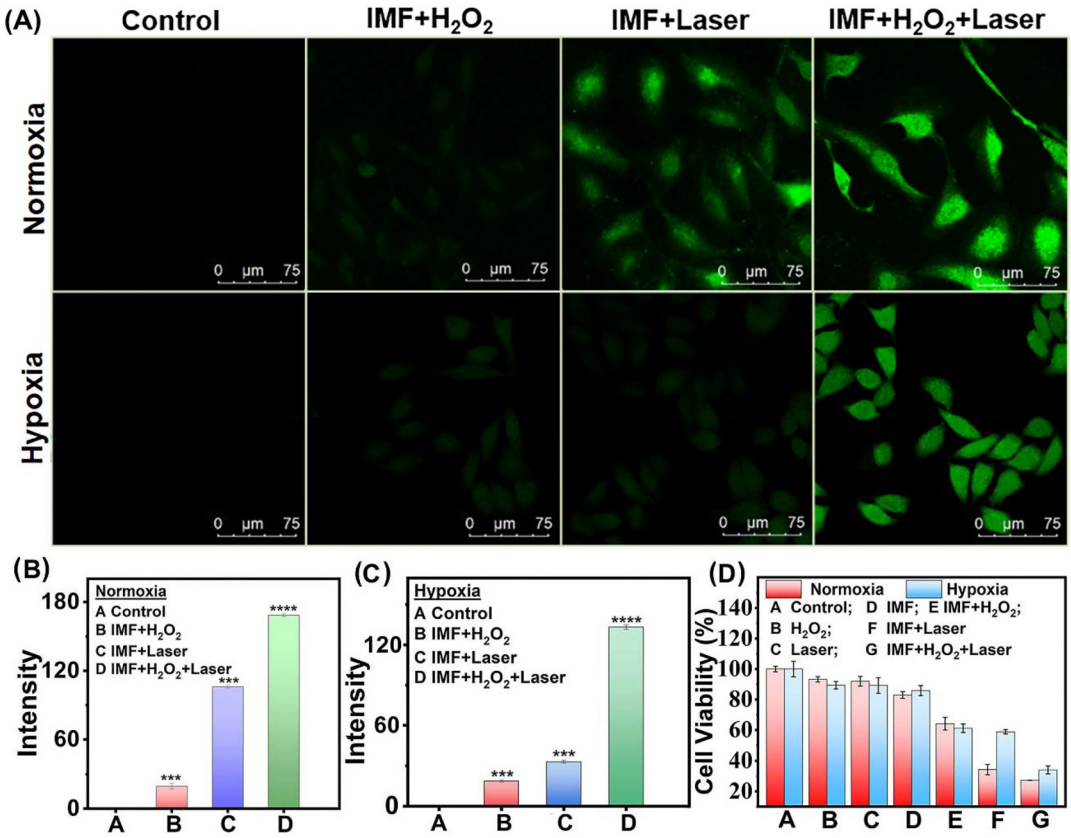

Fig. 4 (A) Confocal images of DCFH-DA-stained HeLa cells with different treatments under normoxia and hypoxia conditions; (B) and (C) the quantifications of fluorescence intensity of DCFH-DA quantified by the data analysis from the confocal microscopy of Fig. 1a. (n = 3), ***p < 0.001, ****p < 0.0001; and (D) MTT assay of HeLa cell viabilities with different treatments under normoxia and hypoxia conditions (laser: 808 nm, 1.5 W cm^{-2}, and 5 min).

 This journal is © the Partner Organisations 2024

Published on 03 oajagemánnu 2024. Downloaded on 2026-02-01 22:11:29.

ence of H_2O_2 under hypoxia conditions compared with the corresponding control groups under normoxia conditions, which demonstrated that the synergetic oxygen generation capacity of FeOOH reinforced by the UMOF significantly improved the $^1O_2$ generation capacity, especially under hypoxia conditions. Additionally, the formation of limited $^{\bullet}OH$ always accompanied by the oxygen generation process based on the Fe^{3+}/Fe^{2+} catalytic cycle has been proved by methylene blue degradation assay (see the ESI for details†), and the weak green fluorescence for $^{\bullet}OH$ was also observed in the dark control groups (Fig. 4A, group IMF + H_2O_2).

In vitro photodynamic performance of IMF

To examine the biocompatibility and photodynamic performance of IMF, MTT assays and confocal fluorescence microscopy studies based on calcein-AM and propidium (PI) co-staining were further performed on the HeLa cells (Fig. 4D and 5). As shown in Fig. 4D, from all the control groups (A–D), we concluded that IMF (200 μg mL^{-1}) itself without H_2O_2 and laser presented good biocompatibility either under normoxia or hypoxia conditions. After H_2O_2 was added in group E without laser, a slight decrease in cell viability was observed both under normoxia and hypoxia conditions, and these should be attributed to the formation of limited $^{\bullet}OH$ always accompanied by the oxygen generation process based on the Fe^{3+}/Fe^{2+} catalytic cycle, which has been demonstrated by the methylene blue degradation assay and ROS confocal fluorescence microscopy (Fig. S20† and Fig. 4A, group IMF + H_2O_2). From group F (IMF + laser) under hypoxic conditions, a slight decrease in cell viability, originated from the hypoxic photodynamic performance of IMF and the supplemented photothermal properties of ICG itself (Fig. S21†), comparable to that for group E (IMF + H_2O_2), has also been observed. In contrast, under normoxia conditions, the cell viability decreased significantly for group F, which further demonstrated the excellent photodynamic performance of IMF with sufficient oxygen conditions. The therapeutic effect far exceeded the sum of both hypoxic PDT and the photothermal compensated by ICG themselves. Then, the optimal experimental results were observed in the experimental group, and especially under hypoxic conditions, the prominent self-oxygen generation performance of IMF significantly improved the efficiency of photodynamic therapy. With laser irradiation under hypoxia conditions, the IC_{50} value of IMF was determined to be 111.6 μg mL^{-1}.

In the confocal fluorescence microscopy studies based on calcein-AM and propidium (PI) co-staining, the optimal photodynamic efficacy was also observed in the experimental groups treated with IMF + H_2O_2 + laser irradiation (Fig. 5). Compared

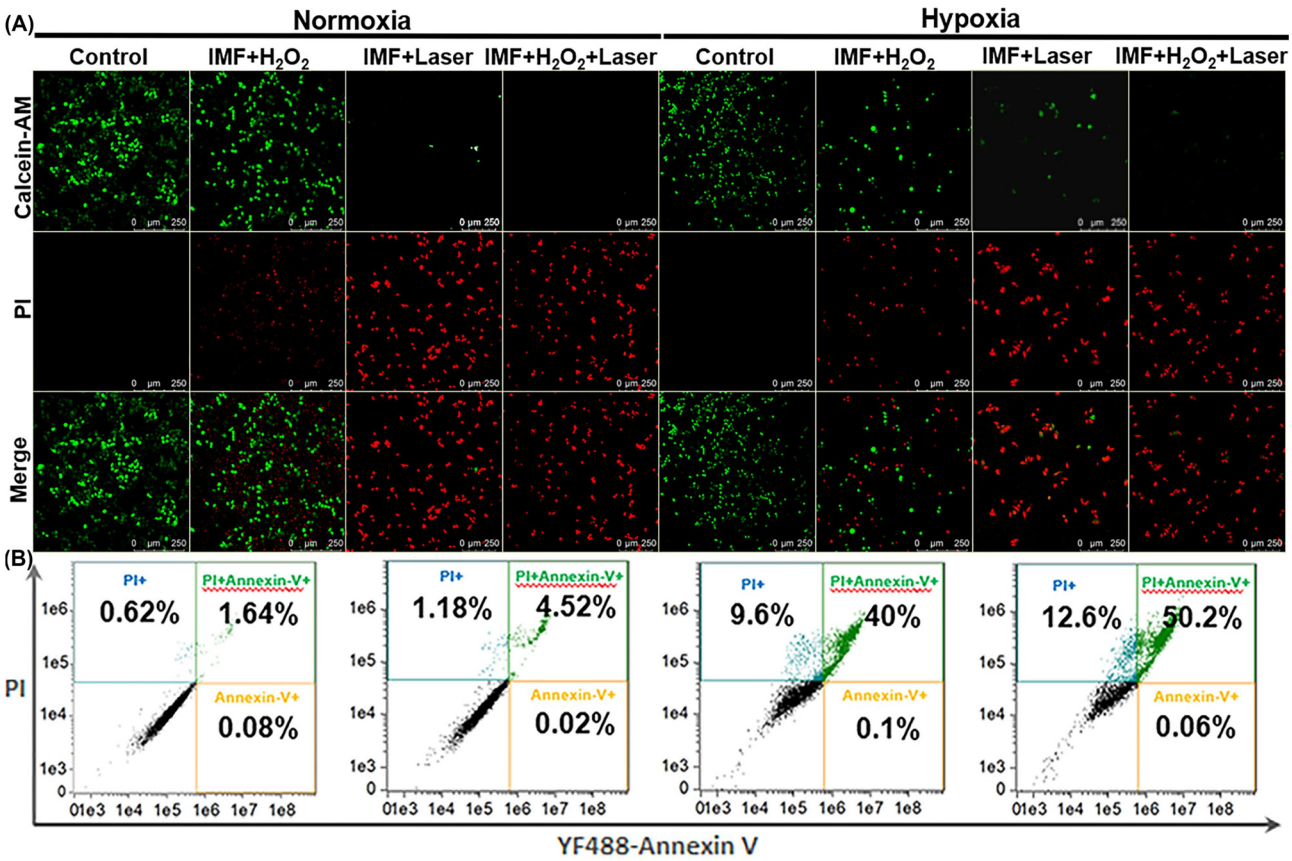

Fig. 5 (A) Confocal images of calcein-AM and PI stained HeLa cells with different treatments under normoxia and hypoxia conditions; and (B) flow cytometry analysis of HeLa cells with corresponding treatments under hypoxia conditions (the cells were stained with PI and annexin V-FITC).

Published on 03 oajagemánnu 2024. Downloaded on 2026-02-01 22:11:29.

with the control groups under normal oxygen conditions, more obvious improvement of photodynamic performance by self-oxygen supply was observed from group IMF + laser and group IMF + H_2O_2 + laser. Under hypoxic oxygen conditions, significant green fluorescence was observed in the group IMF + laser, which should be attributed to the fact that the optimal photodynamic performance has not been achieved. However, under normal oxygen conditions, without limitation of a hypoxic microenvironment, and the photodynamic effect is optimized, resulting in less significant enhancement of the red fluorescent based on self-produced oxygen than that for the hypoxic control groups. Fortunately, after the cells were treated with H_2O_2 in the group of IMF + H_2O_2 + laser, only bright red fluorescence of PI can be observed and the bright green fluorescence of AM in the corresponding IMF + laser group disappeared, intuitively proving the effective self-oxygen generation capacity of IMF could further synergistically improve the photodynamic performance in the hypoxia TEM. Additionally, from the control groups without H_2O_2 and laser, only the bright green fluorescence of AM can be observed, so we also concluded that IMF (200 μg mL^{-1}) itself presented good biocompatibility either under normoxia or hypoxia conditions. The above results of confocal fluorescence microscopy studies under normoxia and hypoxia conditions were consistent with that of MTT assay (Fig. 4D). From flow cytometry experiments shown in Fig. 5B, IMF + H_2O_2, IMF + laser and IMF + H_2O_2 + laser groups were able to induce 5.54%, 40.1% and 50.26% of apoptotic cells, respectively, which further verified the above phenomena. Briefly, the enhanced PDT performance of this novel platform based on a multifunctional MOF under hypoxia conditions was successfully verified using HeLa cells. Additionally, the limited amount of $^{\bullet}OH$ generated simultaneously in the oxygen generation cycle and the photothermal of ICG itself inevitably should have compensated the overall decrease in cell vibility, though the compensated effect is not significant.

In vivo treatment performance of IMF

Motivated by the experimental results *in vitro*, the *in vivo* treatment performance of IMF was examined (Fig. 6). HeLa cells subcutaneous xenograft nude mice were prepared firstly. After reaching a tumor volume of 75–100 mm^3, the nude mice were then divided into three different groups randomly. In the experimental group (IMF + laser), IMF scattered in PBS buffer (c_{ICG} = 0.5 mg kg^{-1}) was injected. The region was then treated with near infrared laser irradiation (808 nm, 1.5 W cm^{-2}) for 5 min. As depicted in Fig. 6B, within the first two days of this treatment, the growth of the tumor for the experimental group has been already significantly inhibited, then it continued to decrease without any treated again. To highlight the signifi-

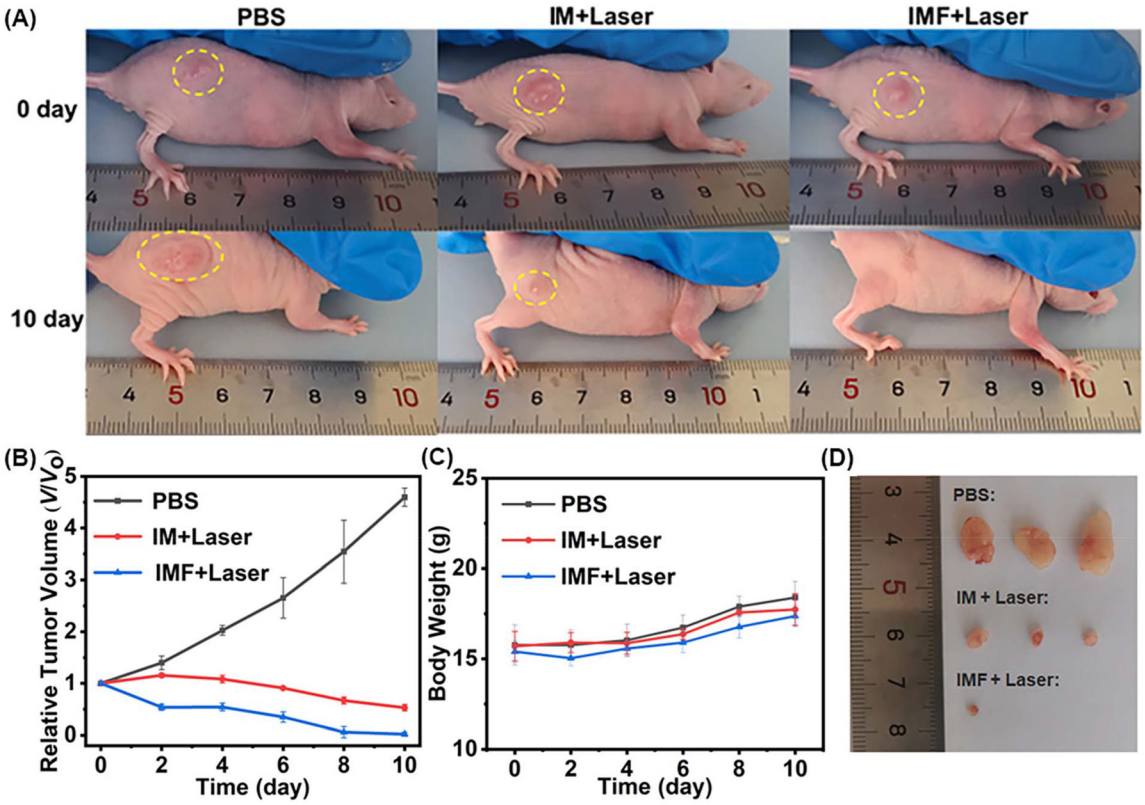

Fig. 6 (A) Photographs of the mice with different treatments; (B) tumor growth inhibition curves after different treatments in the control and experimental groups; (C) body weight curves of the mice with relevant treatments; and (D) photograph of the tumors of the parallel control and experimental groups after the PDT.

 This journal is © the Partner Organisations 2024

Published on 03 oajagemánnu 2024. Downloaded on 2026-02-01 22:11:29.

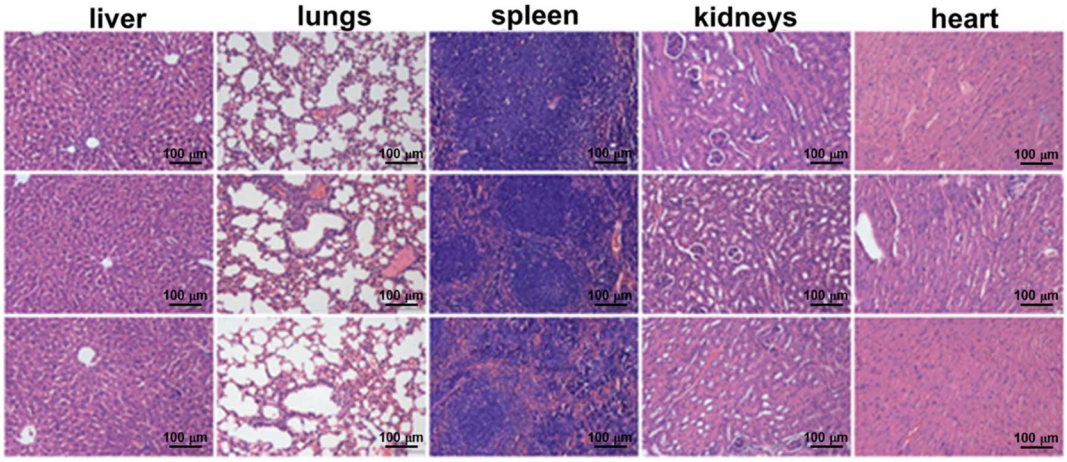

Fig. 7 H&E stained images of tissue sections from different organs of mice 10 days after PDT: PBS only (top row); IMF with irradiation (middle row); and IMF with irradiation (bottom row).

cant compensation effect of the self-oxygen generation performance of IMF and verify the limitation of photodynamic performance caused by the hypoxic microenvironment of solid tumors themselves, ICG ⊂ UiO-66-$(COOH)_2$ (IM) without self-oxygen generation units were prepared. As shown in Fig. 6B, due to the hypoxic microenvironment of solid tumors themselves, in this control group (IM + laser, c_{ICG} = 0.5 mg kg^{-1}, 808 nm, 1.5 W cm^{-2}, 5 min), the tumor growth was not effectively suppressed, which further demonstrated that self-oxygen generation from IMF was indeed able to obviously enhance the efficiency of photodynamic therapy. As depicted in Fig. 6D, among the three tumors in the experimental group, two tumors were completely eradicated. Meanwhile, the body weights of all xenograft nude mice were observed continuously throughout the treatment. As can be seen from Fig. 6C, no obvious changes of body weight were found among the experimental and control groups. Additionally, hematoxylin and eosin (H&E) staining assays of tissue sections from different organs of the corresponding tumor mice after PDT were carried out and no histopathological abnormalities were found in these tissues, indicating good biocompatibility for these novel photosensitive platforms (Fig. 7). Meanwhile, the normal nude mice with intravenous injection of IMF only were further employed to evaluate the compatibility of IMF itself. As depicted in Fig. S22,† the body weights of all nude mice were observed continuously within 5 days and no obvious changes of body weight were found among the experimental and control groups. Besides, H&E stained images of tissue sections from different organs of normal mice after injection of IMF only were also performed and no histopathological abnormalities were observed (Fig. S23†). Overall, based on the hypoxic and high H_2O_2 concentration microenvironment of solid tumors themselves, the effectively enhanced treatment performance of this novel biocompatible platform based on a multifunctional MOF was successfully verified using *in vivo* anti-tumor experiments.

Conclusions

In summary, using a multicarboxyl modification strategy, we for the first time integrated high density biocompatible iron catalase-like active centers and the clinically available ICG molecule into the same MOF platform and obtained a novel self-oxygen generation enhanced photodynamic platform IMF. Moreover, the effectively enhanced PDT performance under hypoxia conditions of this novel platform was successfully verified using HeLa cells and *in vivo* anti-tumor experiments. Overall, this work not only presented a novel photodynamic platform for PDT but also provided an effective construction strategy for conveniently developing a wide variety of water-stable multimetal-based MOFs simultaneously containing large open channels and high density active metal centers.

Author contributions

Guorui Gao and Yifan Wang: investigation, formal analysis, and writing the original draft. Yu Jiang: formal analysis and investigation. Shiping Luo, Mengnan Li and Yanyu Cao: validation and investigation. Yu Ma and Bo Tang: supervision, resources, conceptualization, and writing – review & editing.

Conflicts of interest

There are no conflicts to declare.

Acknowledgements

This work was supported by the National Natural Science Foundation of China (22134004, 21675103 and 21927811), the Taishan Scholars Program of Shandong Province (tsqn.202211102), the Natural Science Foundation of

Published on 03 oajagemánnu 2024. Downloaded on 2026-02-01 22:11:29.

Shandong Province (ZR2022MB006), the Local Science and Technology Development Fund Guided by the Central Government of Shandong Province (YDZX2022012) and the Major Science and Technology Innovation Project of Shandong Province (2021ZDSYS09).

References

1 J. Ouyang, A. Xie and W. Tao, Minimally invasive nanomedicine: nanotechnology in photo-/ultrasound-/radiation-/magnetism-mediated therapy and imaging, *Chem. Soc. Rev.*, 2022, **51**, 4996–5041.

2 M. Ethirajan, Y. Chen, P. Joshi and R. K. Pandey, The role of porphyrin chemistry in tumor imaging and photodynamic therapy, *Chem. Soc. Rev.*, 2011, **40**, 340–362.

3 J. Karges, Clinical development of metal complexes as photosensitizers for photodynamic therapy of cancer, *Angew Chem., Int. Ed.*, 2022, **61**, e202112236.

4 B. Rankin and A. J. Giaccia, Hypoxic control of metastasis, *Science*, 2016, **352**, 175–180.

5 A. L. Maas, S. L. Carter, E. P. Wileyto, J. Miller, M. Yuan, G. Yu, A. C. Durham and T. M. Busch, Tumor Vascular Microenvironment determines responsiveness to photodynamic therapy, *Cancer Res.*, 2012, **72**, 2079–2088.

6 D. Tao, L. Feng, Y. Chao, C. Liang, X. Song, H. Wang, K. Yang and Z. Liu, Covalent organic polymers based on fluorinated porphyrin as oxygen nanoshuttles for tumor hypoxia relief and enhanced photodynamic therapy, *Adv. Funct. Mater.*, 2018, **28**, 1804901.

7 R. A. Day, D. A. Estabrook, J. K. Logana and E. M. Sletten, Fluorous photosensitizers enhance photodynamic therapy with perfluorocarbon nanoemulsions, *Chem. Commun.*, 2017, **53**, 13043–13046.

8 H. Cao, Y. Yang, M. Liang, Y. Ma, N. Sun, X. Gao and J. Li, Pt@polydopamine nanoparticles as nanozymes for enhanced photodynamic and photothermal therapy, *Chem. Commun.*, 2021, **57**, 255–258.

9 W. Pan, Y. Ge, Z. Yu, P. Zhou, B. Cui, N. Li and B. Tang, A cancer cell membrane-encapsulated MnO_2 nanoreactor for combined photodynamic-starvation therapy, *Chem. Commun.*, 2019, **55**, 5115–5118.

10 L. H. Liu, Y. H. Zhang, W. X. Qiu, L. Zhang, F. Gao, B. Li, L. Xu, J. X. Fan, Z. H. Li and X. Z. Zhang, Dual-stage light amplified photodynamic therapy against hypoxic tumor based on an O_2 self-sufficient nanoplatform, *Small*, 2017, **13**, 1701621.

11 C. C. Huang, W. T. Chia, M. F. Chung, K. J. Lin, C. W. Hsiao, C. Jin, W. H. Lim, C. C. Chen and H. W. Sung, An Implantable depot that can generate oxygen in situ for overcoming hypoxia-induced resistance to anticancer drugs in chemotherapy, *J. Am. Chem. Soc.*, 2016, **138**, 5222–5225.

12 D. Jiang, D. Ni, Z. T. Rosenkrans, P. Huang, X. Yan and W. Cai, Nanozyme: new horizons for responsive biomedical applications, *Chem. Soc. Rev.*, 2019, **48**, 3683–3704.

13 S. A. Ansari and Q. Husain, Potential applications of enzymes immobilized on/in nano materials: A review, *Biotechnol. Adv.*, 2012, **30**, 512–523.

14 X. J. Song, J. Xu, C. Liang, Y. Chao, Q. T. Jin, C. Wang, M. W. Chen and Z. Liu, Self-supplied tumor oxygenation through separated liposomal delivery of H_2O_2 and catalase for enhanced radio-immunotherapy of cancer, *Nano Lett.*, 2018, **18**, 6360–6368.

15 I. E. Khalil, J. Fonseca, M. R. Reithofer, T. Eder and J. M. Chin, Tackling orientation of metal-organic frameworks (MOFs): The quest to enhance MOF performance, *Coord. Chem. Rev.*, 2023, **481**, 215043.

16 W. G. Cui, T. L. Hu and X. H. Bu, Metal–Organic Framework materials for the separation and purification of light hydrocarbons, *Adv. Mater.*, 2020, **32**, 1806445.

17 L. B. Li, R.-B. Lin, R. Krishna, H. Li, S. C. Xiang, H. Wu, J. P. Li, W. Zhou and B. L. Chen, Ethane/ethylene separation in a metal-organic framework with iron-peroxo sites, *Science*, 2018, **362**, 443–446.

18 K.-J. Chen, D. G. Madden, S. Mukherjee, T. Pham, K. A. Forrest, A. Kumar, B. Space, J. Kong, Q.-Y. Zhang and M. J. Zaworotko, Synergistic sorbent separation for one-step ethylene purification from a four-component mixture, *Science*, 2019, **366**, 241–246.

19 K. D. Lu, T. Aung, N. N. Guo, R. Weichselbaum and W. B. Lin, Nanoscale Metal–Organic Frameworks for Therapeutic, Imaging, and Sensing Applications, *Adv. Mater.*, 2018, **30**, 1707634.

20 Y. Zhang, S. Yuan, G. Day, X. Wang, X. Yang and H.-C. Zhou, Luminescent sensors based on metal-organic frameworks, *Coord. Chem. Rev.*, 2018, **354**, 28–45.

21 I. Roy and J. F. Stoddart, Cyclodextrin metal–organic frameworks and their applications, *Acc. Chem. Res.*, 2021, **54**, 1440–1453.

22 Y. Zhou, S. T. Liu, Y. M. Gu, G.-H. Wen, J. Ma, J.-L. Zuo and M. N. Ding, In(III) metal–organic framework incorporated with enzyme-mimicking nickel bis(dithiolene) ligand for highly selective CO_2 electroreduction, *J. Am. Chem. Soc.*, 2021, **143**, 14071–14076.

23 F.-K. Shieh, S.-C. Wang, C.-I. Yen, C.-C. Wu, S. Dutta, L.-Y. Chou, J. V. Morabito, P. Hu, M.-H. Hsu, K.C.-W. Wu and C.-K. Tsung, Imparting functionality to biocatalysts via embedding enzymes into nanoporous materials by a de novo approach: size-Selective sheltering of catalase in metal–organic framework microcrystals, *J. Am. Chem. Soc.*, 2015, **137**, 4276–4279.

24 Q. Q. Xing, Y. X. Pan, Y. H. Hu and L. Wang, Review of the biomolecular modification of the metal-organ-framework, *Front. Chem.*, 2020, **8**, 642.

25 L. Jiao, Y. Wang, H.-L. Jiang and Q. Xu, Metal–organic frameworks as platforms for catalytic applications, *Adv. Mater.*, 2018, **30**, 1703663.

26 W. Q. Wang, Y. T. Yu, Y. L. Jin, X. Liu, M. Shang, X. H. Zheng, T. T. Liu and Z. G. Xie, Two-dimensional metal-organic frameworks: from synthesis to bioapplications, *J. Nanobiotechnol.*, 2022, **20**, 207.

 This journal is © the Partner Organisations 2024

Published on 03 oajagemánnu 2024. Downloaded on 2026-02-01 22:11:29.

27 D. W. Feng, Z.-Y. Gu, J.-R. Li, H.-L. Jiang, Z. W. Wei and H.-C. Zhou, Zirconium-metalloporphyrin PCN-222: mesoporous metal–organic frameworks with ultrahigh stability as biomimetic catalysts, *Angew. Chem., Int. Ed.*, 2012, **51**, 10307–10310.
28 K. C. Wang, D. W. Feng, T.-F. Liu, J. Su, S. Yuan, Y.-P. Chen, M. Bosch, X. D. Zou and H.-C. Zhou, A Series of highly stable mesoporous metalloporphyrin Fe-MOFs, *J. Am. Chem. Soc.*, 2014, **136**, 13983–13986.
29 H. J. Cheng, Y. F. Liu, Y. H. Hu, Y. B. Ding, S. C. Lin, W. Cao, Q. Wang and J. J. X. Wu, Monitoring of heparin activity in live rats using metal–organic framework nanosheets as peroxidase mimics, *Anal. Chem.*, 2017, **89**, 11552–11559.
30 Y. Huang, M. T. Zhao, S. K. Han, Z. C. Lai, J. Yang, C. L. Tan, Q.-L. Ma, Q. P. Lu, J. Z. Chen, X. Zhang, Z. C. Zhang, B. Li, B. Chen, Y. Zong and H. Zhang, Growth of Au nanoparticles on 2D metalloporphyrinic metal-organic framework nanosheets used as biomimetic catalysts for cascade reactions, *Adv. Mater.*, 2017, **29**, 1700102.
31 Q. Zheng, X. Liu, Y. Zheng, K. W. K. Yeung, Z. Cui, Y. Liang, Z. Li, S. Zhu, X. Wang and S. Wu, The recent progress on metal–organic frameworks for phototherapy, *Chem. Soc. Rev.*, 2021, **50**, 5086–5125.
32 Y. Ma, X. Li, A. Li, P. Yang, C. Zhang and B. Tang, H_2S-activable MOF nanoparticle photosensitizer for effective photodynamic therapy against cancer with controllable singlet-oxygen release, *Angew. Chem., Int. Ed.*, 2017, **56**, 13752–13756.
33 M. H. Chan, C. H. Li, Y. C. Chang and M. Hsiao, Iron-based ceramic composite nanomaterials for magnetic fluid hyperthermia and drug delivery, *Pharmaceutics*, 2022, **14**, 2584.
34 F. Kievit and M. Zhang, Surface engineering of iron oxide nanoparticles for targeted cancer therapy, *Acc. Chem. Res.*, 2011, **44**, 853–862.
35 Y. Jun, J. Lee and J. Cheon, Chemical design of nanoparticle probes for high-performance magnetic resonance imaging, *Angew. Chem., Int. Ed.*, 2008, **47**, 5122–5135.
36 D. W. Feng, W.-C. Chung, Z. W. Wei, Z.-Y. Gu, H.-L. Jiang, Y.-P. Chen, D. J. Darensbourg and H.-C. Zhou, Construction of ultrastable porphyrin Zr metal–organic frameworks through linker elimination, *J. Am. Chem. Soc.*, 2013, **135**, 17105–17110.
37 M. Y. Li, X. Liu, Y. Che, H. Z. Xing, F. F. Sun, W. Zhou and G. S. Zhu, Controlled partial linker thermolysis in metal-organic framework UiO-66-NH2 to give a single-site copper photocatalyst for the functionalization of terminal alkynes, *Angew. Chem., Int. Ed.*, 2023, **62**, e202308651.
38 A. M. Abdel-Mageed, B. Rungtaweevoranit, M. Parlinska-Wojtan, X. K. Pei, O. M. Yaghi and R. J. Behm, Highly active and stable single-Atom Cu catalysts supported by a metal–organic framework, *J. Am. Chem. Soc.*, 2019, **141**, 5201–5210.
39 P. Jia, Q. S. Wu, B. Y. Sun and L. Wang, Formic acid-regulated defect engineering in Zr-Based metal-organic frameworks toward fluorescence sensor for sensitive detection of chlortetracycline, *Small*, 2023, 2304096.
40 B. B. Guo, X. Y. Cheng, Y. Tang, W. Guo, S. Q. Deng, L. Wu and X. Z. Fu, Dehydrated UiO-66$(SH)_2$: the Zr–O cluster and its photocatalytic role mimicking the biological nitrogen fixation, *Angew. Chem., Int. Ed.*, 2022, **61**, e202117244.
41 J. H. Cavka, S. Jakobsen, U. Olsbye, N. Guillou, C. Lamberti, S. Bordiga and K. P. Lillerud, A new zirconium inorganic building brick forming metal organic frameworks with exceptional stability, *J. Am. Chem. Soc.*, 2008, **130**, 13850–13851.
42 H. Wang, X. Li, B. W.-C. Tse, H. Yang, C. A. Thorling, Y. Liu, M. Touraud, J. B. Chouane, X. Liu, M. S. Roberts and X. Liang, Indocyanine green-incorporating nanoparticles for cancer theranostics, *Theranostics*, 2018, **8**, 1227–1242.
43 Q. Y. Yang, S. Vaesen, F. Ragon, A. D. Wiersum, D. Wu, A. Lago, T. Devic, C. Martineau, F. Taulelle, P. L. Llewellyn, H. Jobic, C. L. Zhong, C. Serre, G. De Weireld and G. Maurin, A water stable metal–organic framework with optimal features for CO_2 capture, *Angew. Chem., Int. Ed.*, 2013, **52**, 10316–10320.
44 J. N. Yao, Y. J. Ji, L. J. Pei, S. F. Tan and F. Y. Ren, Amorphous FeOOH nanoparticles decorated on defect-rich porous Ni MOF nanosheet based hierarchical architectures toward superior OER performance, *New J. Chem.*, 2022, **46**, 9650–9657.
45 C. C. Pei, C. Liu, Y. Wang, D. Cheng, R. X. Li, W. K. Shu, C. Q. Zhang, W. L. Hu, A. H. Jin, Y. N. Yang and J. J. Wan, FeOOH@metal–organic framework core–satellite nanocomposites for the serum metabolic fingerprinting of gynecological cancers, *Angew. Chem., Int. Ed.*, 2020, **59**, 10831–10835.
46 J. Kim, H. R. Cho, H. Jeon, D. Kim, C. Song, N. Lee, S. H. Choi and T. Hyeon, Continuous O_2-evolving $MnFe_2O_4$ nanoparticle-anchored mesoporous silica nanoparticles for efficient photodynamic therapy in hypoxic cancer, *J. Am. Chem. Soc.*, 2017, **139**, 10992–10995.
47 Z. Yang, J. Wen, Q. Wang, Y. Li, Y. Zhao, Y. Tian, X. Wang, X. Cao, Y. Zhang, G. Lu, Z. Teng and L. Zhang, Sensitive, real-time, and *in vivo* oxygen monitoring for photodynamic therapy by multifunctional mesoporous nanosensors, *ACS Appl. Mater. Interfaces*, 2019, **11**, 187–194.
48 E. A. Mayeda and A. J. Bard, Production of singlet oxygen in electrogenerated radical ion electron transfer reactions, *J. Am. Chem. Soc.*, 1973, **95**, 6223–6226.
49 Y. Zhou, W. Xia, C. Liu, S. Ye, L. Wang and R. Liu, A DNA and mitochondria dual-targeted photosensitizer for two-photon-excited bioimaging and photodynamic therapy, *Biomater. Sci.*, 2022, **10**, 1742–1751.